RSC Advances

PAPER

View Article Online
View Journal | View Issue

Cite this: *RSC Adv.*, 2024, **14**, 8366

The dual-model up/down-conversion green luminescence of $NaSrGd(MoO_4)_3$: Er^{3+} and its application for temperature sensing†

Zein El Abidine Aly Taleb, Kamel Saidi * and Mohamed Dammak

Er^{3+}-doped phosphors are widely used as dual-functional optical thermometers due to their distinctive up/down-conversion luminescence and the thermally coupled energy states ($^2H_{11/2}$ and $^4S_{3/2}$) of Er^{3+}. The development of high-performance Er^{3+}-activated optical thermometers is both an intriguing subject and a formidable challenge in the field. This article investigates the up/down-conversion (UC and DC) photoluminescence properties of $NaSrGd(MoO_4)_3$ (NSGM): Er^{3+}. When excited at 375 and 975 nm, the phosphors emit peaks at 530, 550, and 657 nm, corresponding to the $^2H_{11/2}$, $^4S_{3/2}$, and $^4F_{9/2} \rightarrow {}^4I_{15/2}$ transitions of Er^{3+}, with the $^4S_{3/2} \rightarrow {}^4I_{15/2}$ transition displaying the highest intensity. The optical properties are comprehensively studied through UV-visible absorption, PL spectroscopy, and PLE spectroscopy. Optimal luminescence intensity is achieved at an Er^{3+} concentration of 4% mol. The resulting chromatic coordinates (x, y) and high correlated color temperature (CCT) values of the doped phosphors yield thermally stable cold emissions in the green region, boasting color purities of approximately 98.76% and 80.74% for DC and UC conversion, respectively. The optical temperature sensing properties of thermally coupled energetic states are explored based on the fluorescence intensity ratio principle. NSGM: $0.04Er^{3+}$, under 375 nm light excitation, demonstrates the maximum relative sensitivity of $0.87\%/K^{-1}$ at 298.15 K, spanning a wide temperature range from 298.15 to 488.15 K. Conversely, under 975 nm light excitation, NSGM: $0.04Er^{3+}$ exhibits the maximum relative sensitivity of $0.63\%/K^{-1}$ over the same temperature range, with temperature uncertainty (δT) less than 0.50 K and repeatability (R) (more than 98%). These findings position this material as a promising candidate for optical thermometer applications. The optical heating capacity of the synthesised phosphor is also determined using optical thermometry results, and heat generation up to approximately 457 K is found, indicating that NSGM: $0.04Er^{3+}$ could be useful for photo-thermal therapy.

Received 5th February 2024
Accepted 6th March 2024

DOI: 10.1039/d4ra00934g

rsc.li/rsc-advances

I. Introduction

Researchers are currently highly motivated by the development of new phosphorescent materials due to their diverse applications in fields such as solid-state lighting, display devices, bio-imaging, latent fingerprint detection, non-contact temperature sensing, solar cells, and indoor plant growth.[1–3] As a result, the development of an effective phosphorescent material using a suitable host and ion activator is still a pressing need. Phosphorescent materials can be broadly categorized into up/down-converting phosphorescent, where the former converts high-energy photons into low-energy ones, and the latter does the opposite. Compared with other rare earth-doped luminescent matrix materials, molybdate has been proposed as a highly efficient luminescent material owing to its significant properties of good chemical stability, high quantum yield, and versatile morphology. These materials exhibit broad and intense absorption bands in the near-UV region, primarily attributed to charge transfer (CT) transitions.[4–8] The NSGM is highly regarded as an excellent luminescent material capable of efficient up/down-conversion emission. This is due to its stable physical and chemical properties, as well as its notably low phonon energy.[8–11] Notably, rare earth ions, particularly Er^{3+} ions introduced into a suitable host, exhibit two highly intense emission peaks at around 530 and 550 nm under both UV and near-infrared excitations.[12–16] Consequently, Er^{3+} ions can serve as effective activators, and NSGM molybdates are ideal hosts for the development of green phosphorescent materials. In addition to these considerations, the quest for DC and UC phosphor materials for high-temperature thermometry with enhanced accuracy poses a significant challenge for researchers. The challenge arises from the thermal quenching of emission in high-temperature conditions.[17–21] Within this context, our article explores the realm of non-contact temperature sensing,

Laboratoire de Physique Appliquée, Groupe des Matériaux Luminescents, Faculté des Sciences de Sfax, Département de Physique, Université de Sfax, BP 1171, Sfax, Tunisia. E-mail: saidikamel494@gmail.com

† Electronic supplementary information (ESI) available. See DOI: https://doi.org/10.1039/d4ra00934g

an essential parameter that demands precise regulation in various scientific experiments. Traditional thermometers necessitate direct contact with the object under measurement, rendering them ineffective in a multitude of challenging and remote situations, such as high-temperature reactors, hazardous radiation zones, underground mines, and fast-moving objects. To address these limitations, the article discusses the potential of non-contact optical thermometers, which rely on the fluorescence intensity ratio (FIR) of two luminescence peaks, offering a reliable solution to the problem. The FIR method is based on the ratio of luminescence intensities from either thermally coupled energy levels of a single activator ion or non-thermally coupled energy levels of two activator ions. The key advantage of FIR-based thermometers lies in their high accuracy, as they are independent of the excitation source and external factors.[22–26] The existence of two thermally coupled energy levels, specifically $^2H_{11/2}$ and $^4S_{3/2}$ of Er^{3+} ions enable their application in temperature sensing scenarios. In this study, NSGM was chosen as the matrix due to its simple preparation, high physical stability and environmental friendliness. Er^{3+} ions were used as activators. DC and UC photoluminescence emission spectra, excited by UV light at 375 nm and near-infrared radiation at 975 nm respectively, as well as sensitivities related to temperature detection, were investigated in depth. Therefore, the NSGM: Er^{3+} phosphor described in this article holds promise for temperature sensing applications. The optical heating capacity of the synthesized phosphorus is also determined using optical thermometry results, and heat generation is found, indicating that NSGM: Er^{3+} could be useful for photo-thermal therapy.

II. Experimental section

The solid-state reaction method was adopted to synthesize a series of erbium Er^{3+}-doped NSGM materials. The raw materials, namely Na_2CO_3, $SrCO_3$, Gd_2O_3, Er_2O_3 and MoO_3, were used in appropriate proportions. All precursors were carefully sampled, ground with an agate mortar and then calcined at 673 K for 8 hours. They were then cooled, ground again and compressed into 8 mm diameter pellets using a stainless-steel mold. The pellets were then heated at a temperature of 1273 K for a period of 12 hours. All chemical reagents used in this study were purchased from Sigma-Aldrich and employed without the need for further purification steps. The chemical reaction formula is as follows:

$$Na_2CO_3 + 2SrCO_3 + (1 - x)Gd_2O_3 + xEr_2O_3 + 6MoO_3 \rightarrow 2NaSrGd_{1-x}Er_x(MoO_4)_3 + 3CO_2$$

III. Characterization techniques

The powder X-ray diffraction (PXRD) patterns of the sample were performed at room temperature using a powder X-ray D8-Advance Bruker diffractometer, with monochromatic copper radiation $CuK\alpha_1$ (1.5406 Å) on the 20–80 2θ degree range. The samples' morphologies were examined using a Zeiss Supra55VP FEG-SEM and Bruker XFlash 5030. UV-vis-NIR absorption was determined using a UV-vis-NIR spectrometer (PerkinElmer Lambda 365). Photoluminescence excitation (PLE) and photoluminescence (PL) spectra investigations were carried out in Fluoromax 4 P model Horiba spectrometer equipped with a xenon lamp as the excitation source at room temperature. For the optical thermometry study, the sample are placed inside a homemade nano heater chamber having controlled heating with an accuracy of ± 0.5 K. Through 375 nm and 975 nm diode laser excitations at constant pump power of 30 mW the emission spectra were recorded on monochromator (Horiba Jobin Yvon, iHR320) spectrometer. The monochromator uses an 1800 g per mm grating blazed at 500 nm and a photomultiplier tube (Hamamatsu, R928) to measure luminescence in the green (520–570 nm) emission bands. The temperature of the sample was varied from room temperature to 488.15 K with the interval of 10 K.

IV. Result and discussion

1. X-ray diffraction analysis

X-ray diffraction (XRD) patterns were used to study the crystal structure and phase purity of the samples. Fig. 1(a) shows XRD patterns of NSGM: $x\mathrm{Er}^{3+}$ microcrystals (with $x = 0.02$, 0.04, 0.06 and 0.08) in the 20–80 $2\theta^\circ$ range. According to these NSGM XRD diagrams (JCPDS no. 70-0257), the samples exhibit a tetragonal structure with a space group $I4_1/a$ (88), which is isomorphic with $CaMoO_4$.[27] The peaks are precisely indexed and no additional peaks are observed in the XRD diagram. This indicates that the prepared luminophores have a single-phase formation, confirming the successful incorporation of the Er^{3+} ion into the Gd^{3+} site. The X-ray diffraction peak shifts to the right because the ionic radii of Er^{3+} ($r = 0.1062$ nm) is smaller than that of Gd^{3+} ($r = 0.107$ nm). In addition, Rietveld refinement (Fig. S_1†) was used to check the structural parameters (space group and cell parameters), and Table S_1† shows the lattice parameters and corresponding unit cell volumes of the synthesized luminophores. Fig. 1(b) displays SEM micrographs of NSGM: 0.04% Er^{3+}. The micrographs reveal particles with irregular shapes that tend to aggregate. These particles have sizes in the micrometer range, approximately 2 μm.

2. Optical properties

2.1. UV absorption spectroscopy. The diffuse reflectance spectra of NSGM: $0.04\mathrm{Er}^{3+}$ phosphors in the 200–1100 nm range is shown in Fig. 2(a); the spectra show a broad absorption band around 320 nm, attributed to electronic transitions of the (MoO_4) group.[28] The other absorption bands around 380, 406, 450, 488, 530, 657, 801 and 975 nm, which are attributed to the $^4I_{15/2} \rightarrow {}^4G_{11/2}$, $^4I_{15/2} \rightarrow {}^2H_{9/2}$, $^4I_{15/2} \rightarrow {}^4F_{5/2}$, $^4I_{15/2} \rightarrow {}^4F_{7/2}$, $^4I_{15/2} \rightarrow {}^2H_{11/2}$, $^4I_{15/2} \rightarrow {}^4F_{9/2}$, $^4I_{15/2} \rightarrow {}^4I_{9/2}$, and $^4I_{15/2} \rightarrow {}^4I_{11/2}$ electron transitions, respectively, of Er^{3+} ions. Kubelka and Munk[30] propounded the calculation of the band gap of a material using the diffuse reflectance spectrum. Can be calculated by using the Kubelka–Munk (K–M) function and

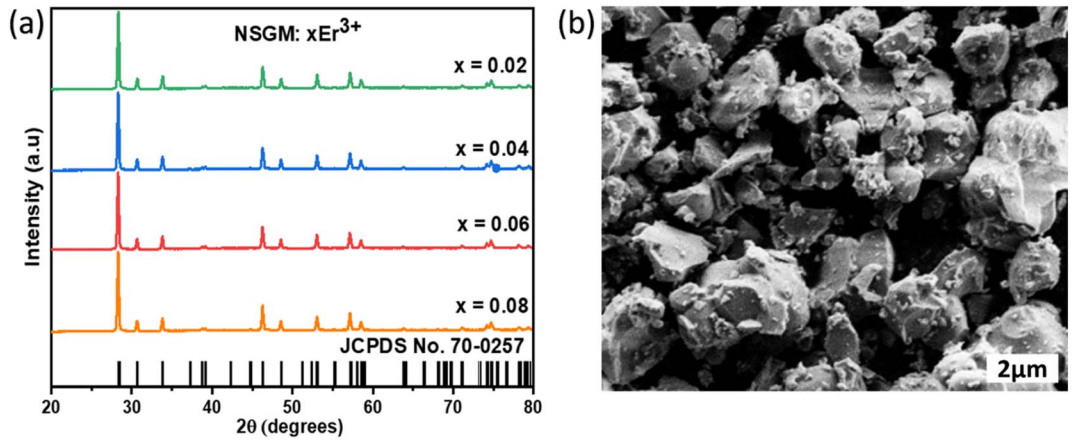

Fig. 1 (a) XRD of the NSGM: $x\mathrm{Er}^{3+}$ (x = 0.02, 0.04, 0.06 and 0.8), (b) SEM image of NSGM: $0.04\mathrm{Er}^{3+}$.

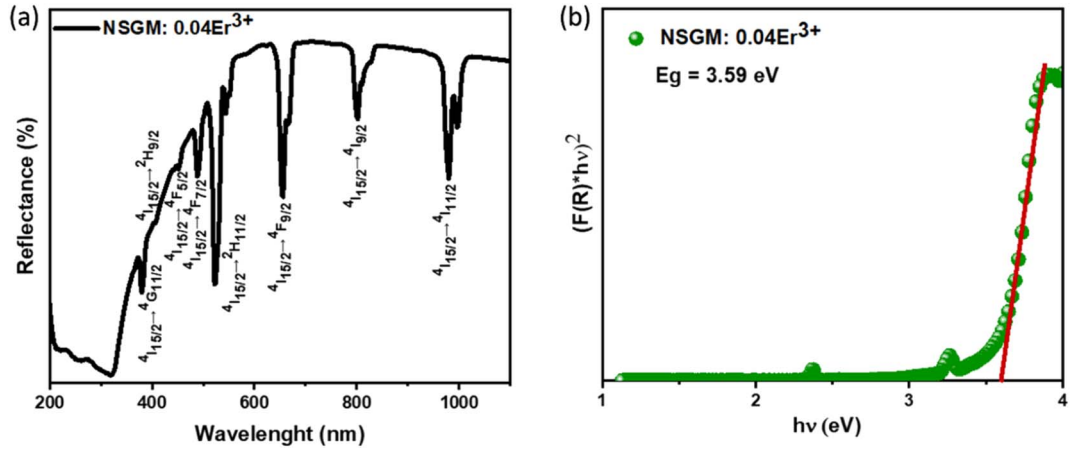

Fig. 2 (a) Diffuse reflectance spectra and (b) the plot of $[F(R)h\nu]^2$ *versus* ($h\nu$) of NSGM: $0.04\mathrm{Er}^{3+}$.

the Tauc relationship and can be written by the following expression:[29]

$$[F(R)_{\infty}h\nu] = B(h\nu - E_g)^n \quad (1)$$

where, B is the proportionality constant and n is a constant that characterizes the nature of the band transition which can have values n = 1/2 or 2 for direct or indirect band transitions, respectively. The plot is displayed in Fig. 2(b). Prior literature affirms that NSGM is a direct band gap material,[30] and its estimation is based on plotting $[F(R)h\nu]^2$ as a function of $h\nu$ for a direct band gap transition. From the graph of $[F(R)h\nu]^2$ *versus* $h\nu$, the value of E_g was extracted by extrapolating the linearly fitted regions until $[F(R)h\nu]^2$ reached zero. The band gap for NSGM: $0.04\mathrm{Er}^{3+}$ is calculated to be 3.59 eV, which is close to values observed in previous reports.[6]

2.2. Down and up-conversion photoluminescence. To gain a deeper understanding of the potential of the produced powder as a new phosphor, a thorough and systematic analysis of the excitation and photoluminescence emission of Er^{3+}-doped NSGM was conducted. Fig. 3(a) shows the DC excitation spectrum of NSGM: 0.04 Er^{3+} microcrystals, measured by monitoring the emission at 545 nm. This spectrum shows a broad band and several narrow peaks. The broad excitation band ranging from 250 to 350 nm with a central wavelength of about 304 nm was attributed to the charge transfer band (CTB) from the fully filled 2p orbitals of oxygen ions to the partially filled 5d orbitals of molybdenum ions.[31,32] And the narrow peaks located at about 365, 378, 406, 450, and 488 nm which correspond to the spin forbidden 4f–4f transitions of Er^{3+} ions from the ground state of $^4I_{15/2}$ to $^4G_{9/2}$, $^4G_{11/2}$, $^2H_{9/2}$, $^4F_{5/2}$, and $^4F_{7/2}$, respectively.[33,34] This novel phosphor can be well excited by UV (200–500 nm), suggesting that the Er^{3+}-activated NSGM are promising candidates for solid-state lighting as green-emitting phosphors. Furthermore, the DC emission spectrum is formed by two intense green emissions at 530 and 550 nm corresponding to the $^2H_{11/2} \rightarrow {}^4I_{15/2}$, $4S_{3/2} \rightarrow {}^4I_{15/2}$ transitions of Er^{3+} ions, respectively, and a faint red emission at about 657 nm, which was attributed to the $^4F_{9/2} \rightarrow {}^4I_{15/2}$ transition,[35] as shown in Fig. S_2(b).† The observed emission bands were consistent with those found in other luminescent materials Er^{3+} ions-based.[36,37]

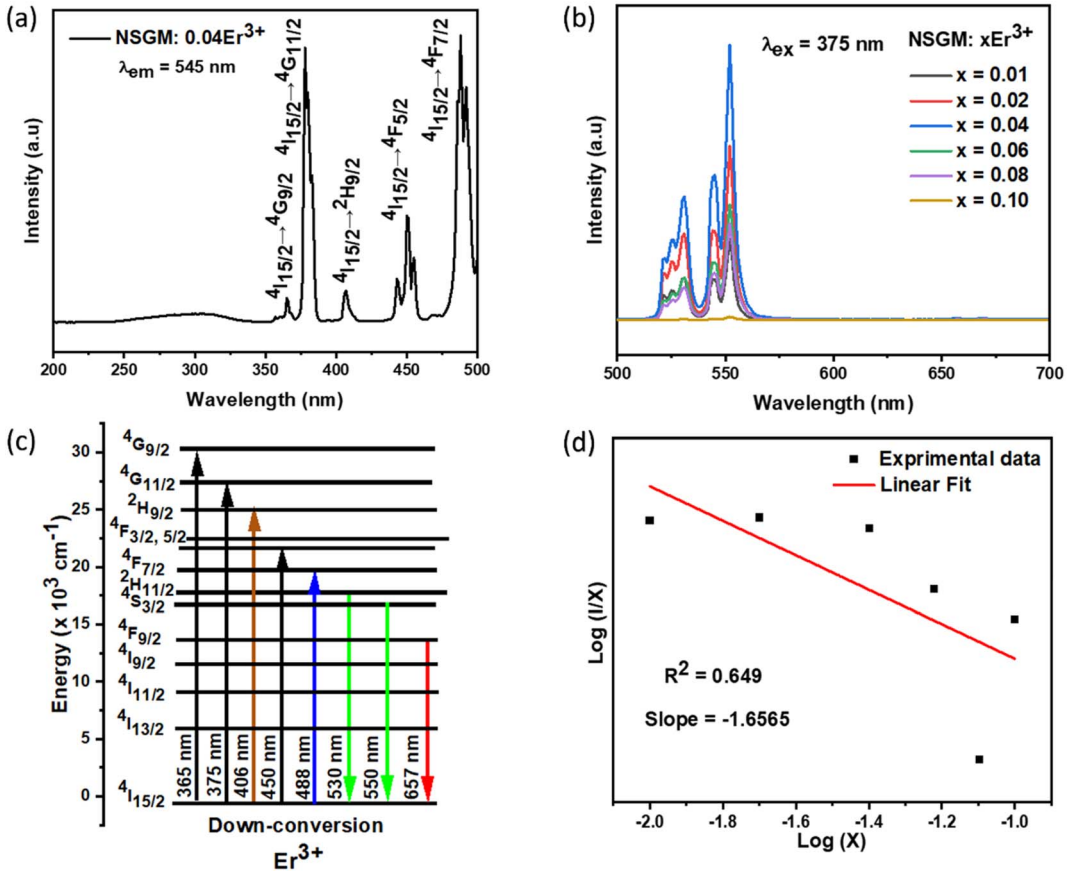

Fig. 3 (a) Excitation spectra monitored at $\lambda_{em} = 545$ nm of NSGM: 0.04Er^{3+}; (b) emission spectrum of NSGM: $x$$Er^{3+}$ excited at 375 nm; (c) the energy level diagram Er^{3+} ion showing the energy transfer process in down-conversion mechanism and (d) relations between the log(I/x) and log(x) in NSGM: $x$$Er^{3+}$.

Fig. 3(b) shows the DC emission spectra of NSGM: $x$$Er^{3+}$ (x = 0.01, 0.02, 0.04, 0.06, and 0.08 and 0.10) recorded at the excitation wavelength of 375 nm. Two light emission peaks are present at 530 and 550 nm in the green region, and a faint peak is present in the red region at 657 nm. These are the characteristic emission peaks of Er^{3+} ions, and the electronic transitions responsible for these peaks are $^2H_{11/2} \rightarrow {}^4I_{15/2}$ (530 nm), $^4S_{3/2} \rightarrow {}^4I_{15/2}$ (550 nm) and $^4F_{9/2} \rightarrow {}^4I_{15/2}$ (657 nm).[38–40] Fig. 3(c) shows a schematic representation of the energy levels of the Er^{3+} ion and the electronic transitions involved in the excitation and emission phenomena. When the material is excited at 375 nm, the electrons of Er^{3+} ions go from the ground state $^4I_{15/2}$ to the excited state $^4G_{11/2}$. The electrons then relax non-radiatively to the $^2H1_{1/2}$, $^4S3/2$ and $^4F_{9/2}$ states. Then the radiative transitions $^2H_{11/2} \rightarrow {}^4I_{15/2}$ (530 nm), $^4S_{3/2} \rightarrow {}^4I_{5/2}$ (550 nm), and $^4F_{9/2} \rightarrow {}^4I_{15/2}$ (657 nm) take place. We can see from Fig. 3(b) that the change in doping percentage does not affect the position of the emission peaks. However, the emission becomes brighter as the doping percentage increases from 1% to 4% mol Er^{3+}. The brightest emission is observed at 4% mol Er^{3+} ion doping. A further increase in the doping level reduces the brightness of the material due to the concentration quenching effect. The type of interaction between Er^{3+} ions that causes the concentration quenching effect. This could be realized by evaluating the critical energy transfer distance (R_c):[41,42]

$$R_c = 2 \times \left[\frac{3V}{4\pi X_c Z}\right]^{1/3} \quad (2)$$

The formula for the critical distance of Er^{3+} ions in NSGM arrays is approximately $R_c = 15.76$ Å, indicating the involvement of the electric multipolar interaction. To better understand the energy transfer mechanism in NSGM: $x$$Er^{3+}$, the following equation, suggested by Dexter, is provided:[43–45]

$$\frac{I}{X} = k\left(1 + \beta(X)^{\theta/3}\right)^{-1} \quad (3)$$

The electric multipole interaction includes dipole–dipole, dipole-quadrupole and quadrupole–quadrupole interactions, using (eqn (3)). The type of energy transfer mechanism can be identified by analyzing the value of θ in the relationship between luminescence intensity (I) and doping concentration (X). Fig. 3(d) illustrates a linear relationship between log(I/X) and log(X), where the slope of the fitted straight line is −1.6565. The value of θ is found to be 4.9, which is approximately the

same as the value of 6. This demonstrates that the non-radiative energy transfer between Er^{3+} ions in the NSGM host lattice is primarily governed by the electric dipole–dipole (d–d) interaction. Fig. 3(b) illustrates the electron transition process of DC emission when excited by a 375 nm wavelength. Under a 375 nm ultraviolet excitation, electrons are excited to the $^4G_{11/2}$ state and subsequently return to the ground state through a relaxation process. This results in the narrowband luminescence characteristic of the Er^{3+} 4f–4f luminescence in the visible region, as determined by previous reports and the energy levels of Er^{3+} ions.

Contrary to most prior publications, Er^{3+} was able to obtain self-activated UC luminescence in the absence of Yb^{3+} in this study. In the matching UC spectra, a green band comprising two emission peaks situated at 530 and 550 nm can be seen (Fig. 4(a)), which are ascribed to Er^{3+} 4f–4f electronic transitions: $^2H_{11/2}$, $^4S_{3/2} \rightarrow {}^4I_{15/2}$.

The optimal doping ion concentration is found to be 4% mol Er^{3+}, which is comparable to the luminescence behavior stimulated by 375 nm. UC luminescence is a nonlinear process whose luminous intensity (I_{UC}) and pump power (P) meet the relationship:[46,47]

$$I_{UC} = P^n \quad (4)$$

where n is the number of pumping photons necessary to excite the electron of the luminescent ion from the ground state to the excited state.[37] The linear fitting of a two-log plot of UC luminescence intensity (Fig. 5) and pump power yields the value of n. Fig. 5 depicts the two emission peaks (530 and 550) of the NSGM: $0.04Er^{3+}$ sample, with slopes computed at 530 and 550 nm, respectively, suggesting that a two-photon process produced the UC luminescence.

It should be mentioned that both the excited state absorption (ESA) of Er^{3+} and the energy transfer (ET) between Er^{3+} were the primary sources of the green and red UC emissions. Er^{3+} was initially excited by a 975 nm photon, transitioning from the ground state $^4I_{15/2}$ level to the $^4I_{11/2}$ level, or GSA: $^4I_{15/2}$ + a photon $\rightarrow {}^4I_{11/2}$. Subsequently, this Er^{3+} may absorb another 975 nm photon (ESA process) or transmit its energy to another Er^{3+} (ET process) in the $^4I_{11/2}$ level, resulting in the population of $^4F_{7/2}$ level of Er^{3+}. Next, the non-radiative relaxation of the Er^{3+} at the $^4F_{7/2}$ level leads to the $^2H_{11/2}$ levels ($^4F_{7/2} \rightarrow {}^2H_{11/2}$ + phonons). Ultimately, the presence of both $^2H_{11/2}$ and $^4S_{3/2}$ levels in a state of thermal equilibrium allows for the acquisition of green emissions from these levels ($^2H_{11/2}$, $^4S_{3/2}$) $\rightarrow {}^4I_{15/2}$ + photon). Additionally, because of the short energy gap between these two energy levels, the excited Er^{3+} in the $^4I_{11/2}$ level can nonradiatively relax to the $^4I_{13/2}$ level *via* a multi-phonon relaxation process. The Er^{3+} in $^4I_{13/2}$ level can absorb energy from another Er^{3+} in $^4I_{11/2}$

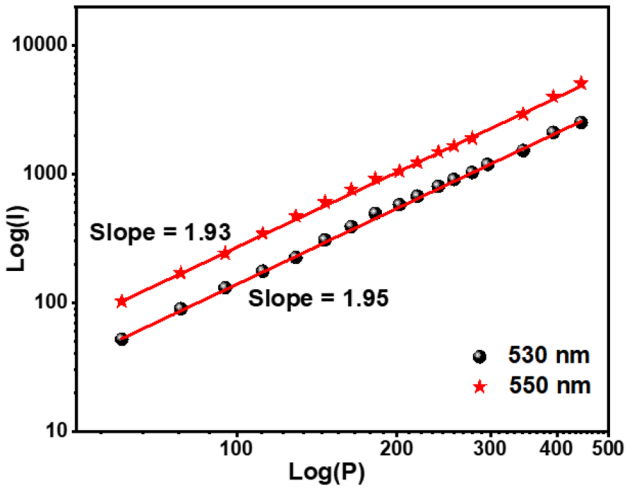

Fig. 5 Log(I) *versus* log(P) plot of 530 and 550 nm peaks of NSGM: $0.04Er^{3+}$.

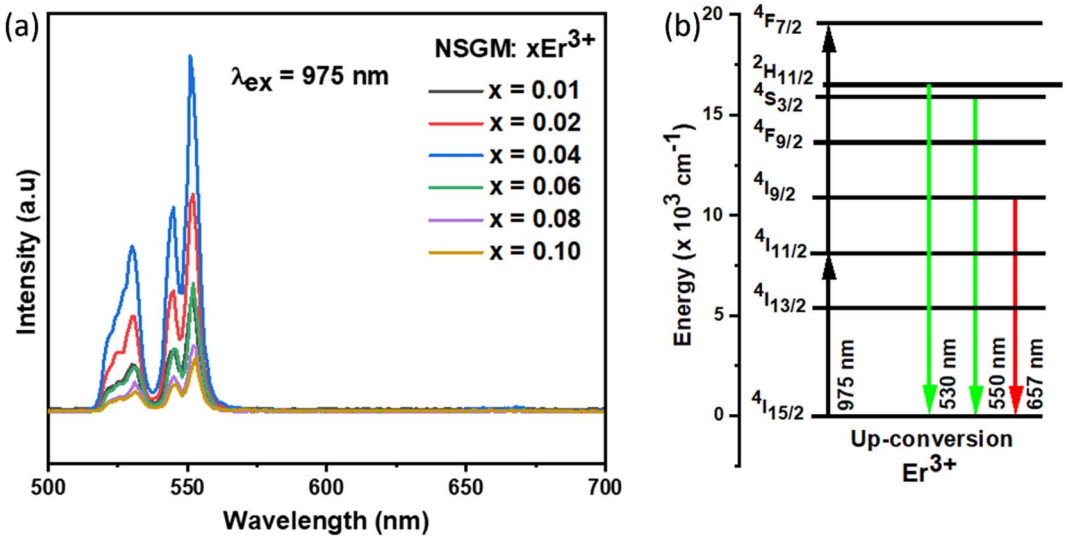

Fig. 4 (a) Emission spectrum of NSGM: xEr^{3+} (x = 0.01, 0.02, 0.04, 0.06, 0.08 and 0.10) excited at 975 nm; (b) the energy level diagram Er^{3+} ion showing the energy transfer process in down-conversion mechanism.

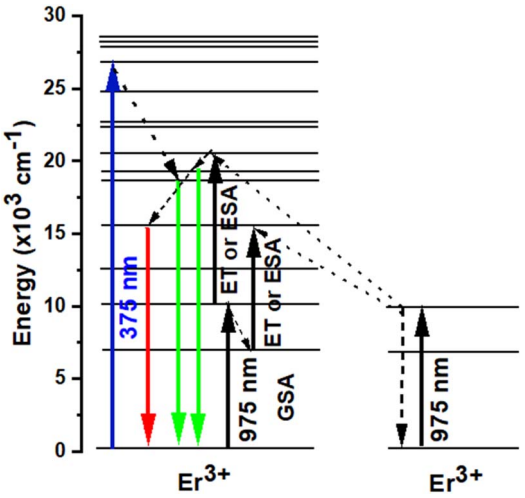

Fig. 6 Energy level diagrams of Er^{3+} and the possible DC and UC luminescence mechanisms of NSGM: 0.04Er^{3+} sample under 375 nm and 975 nm excitations.

through an ET process or an ESA process to reach the $^4F_{9/2}$ level. A $^4F_{9/2} \rightarrow {}^4I_{15/2}$ transition can subsequently produce the red emission (Fig. 6).[48–52]

2.3. Photometric analysis. The photometric study explores the color appearance (chromaticity coordinates), color purity (CP) and correlated color temperature (CCT) of the light emitted by the synthesized material. Fig. 7(a) and (b) illustrates the CIE chromaticity representations obtained for (DC) and (UC) of NSGM: 0.04Er^{3+} at room temperature, respectively. The CIE coordinates are in the green region. The position of the CIE coordinates suggests that the synthesized material has good color purity. Color purity indicates the degree of monochromaticity of the light. We also assessed the purity of the colors using the following relationship:[40,53]

$$C_p = \frac{\sqrt{(x - x_i)^2 (y - y_i)^2}}{\sqrt{(x_d - x_i)^2 (y_d - y_i)^2}} \times 100\% \quad (5)$$

where (x, y), (x_i, y_i), and (x_d, y_d) represent color coordinate, white light points and dominant wavelength point, respectively. CCT of phosphor material is equal to the temperature of an ideal body radiator that emits the light of the same chromaticity as the phosphor does. McCamy formula is followed to determine the CCT of the light emitted from the synthesized materials:[40,53]

$$CCT = -437n^3 + 3526n^2 - 6823n + 5520.23 \quad (6)$$

where $n = (x - x_e)/(y - y_e)$ and $x_e = 0.3320$, $y_e = 0.1858$. The computed values for color coordinates and correlated color temperature (CCT) are determined to be approximately ($x = 0.276$, $y = 0.673$, and CCT = 6343 K) for DC, and ($x = 0.359$, $y = 0.607$, and CCT = 5092 K) for UC. Moreover, the calculated color purity (CP) is found to be approximately 98.76% and 80.74% for DC conversion and UC conversion, respectively. The fact that the CCT values exceed 5000 K and the CP values surpass 80% indicates that the suggested material has the potential to be a green phosphor suitable for cold white-LEDs. Notably, chromaticity coordinates (x, y) of the DC phosphors are most close to pure green emission. The color purity of the sample was estimated and reached a maximum value of 98.76%, indicating the high pure green light emission of the obtained phosphor. Overall, the high color purity of the UC and DC phosphor suggest that it is suitable as a candidate material for optoelectronic devices.

2.4. Temperature-sensing properties of NSGM: Er^{3+}

2.4.1. Temperature-dependent DC photoluminescence and temperature sensing. Due to the small energy separation between the thermally coupled $^2H_{11/2}$ and $^4S_{3/2}$ levels of Er^{3+} ions, the $^2H_{11/2}$ level can be populated from the $^4S_{3/2}$ level through thermal excitation and reach thermal quasi-equilibrium. This leads to varying FIR values in the green emissions of the $^2H_{11/2} \rightarrow {}^4I_{15/2}$ and $^4S_{3/2} \rightarrow {}^4I_{15/2}$ transitions of Er^{3+} ions at different temperatures.[54,55] This characteristic makes luminescent materials based on Er^{3+} ions suitable for non-invasive optical temperature sensors using the FIR technique. To investigate the feasibility of the synthesized compounds for non-contact thermometry, the temperature-dependent PL emission spectra of NSGM: 0.04Er^{3+} microcrystal were recorded in the temperature range of 298.15–488.15 K under 375 nm excitation. As shown in the figure, the position of the emission bands remains constant

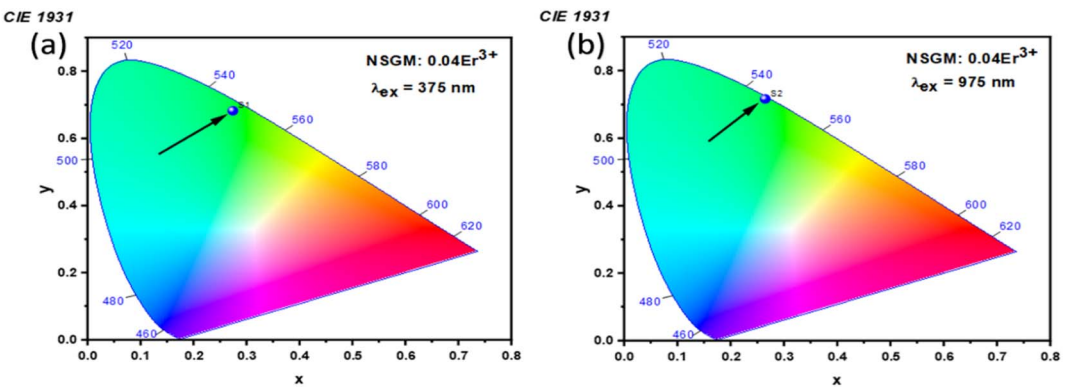

Fig. 7 (a) and (b) Shows the CIE chromatic diagram of NSGM: 0.04Er^{3+} at excitations of 375 nm and 975 nm, respectively.

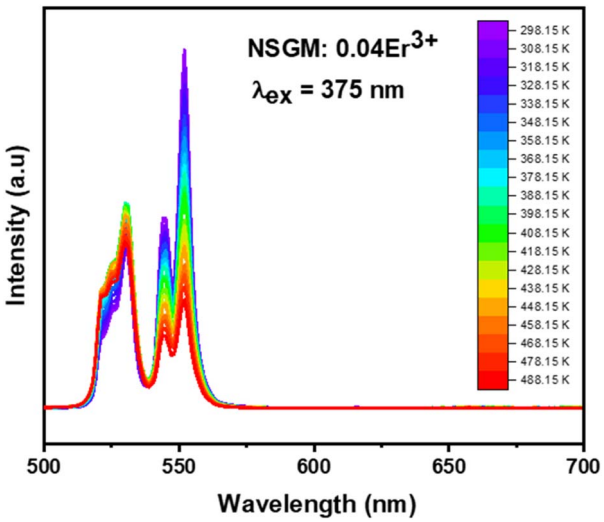

Fig. 8 Temperature-dependent down-conversion photoluminescence emission spectra of NSGM: 0.04 Er^{3+} under 375 nm excitation.

with temperature, while the emission intensities gradually decrease due to thermal quenching effects. It is worth noting that the emission intensity from the $^4S_{3/2} \rightarrow {}^4I_{15/2}$ transition is stronger than that from the $^2H_{11/2} \rightarrow {}^4I_{15/2}$ transition at lower absolute temperatures, whereas the opposite phenomenon is observed at higher temperatures (refer to the Fig. 8). This further indicates that the population between the $^2H_{11/2}$ and $^4S_{3/2}$ levels can be redistributed at elevated temperatures, and the ($^2H_{11/2}$, $^4S_{3/2}$) levels are thermally coupled.

By utilizing the temperature-dependent PL emission spectra, the FIR values of the green emissions were calculated.

The corresponding results are presented in the Fig. 9(a). According to previous literature, the relative population of thermally coupled levels (TCL) ($^2H_{11/2}$, $^4S_{3/2}$) follows the Boltzmann distribution and their FIR can be expressed as follows:[54,56]

$$\mathrm{FIR} = \frac{I_H}{I_S} = B\ \exp\left(\frac{-\Delta E}{kT}\right) \quad (7)$$

where, I_H and I_S represent the integrated emission intensities for the $^4H_{11/2} \rightarrow {}^4I_{15/2}$ (530 nm) and $^4S_{3/2} \rightarrow {}^4I_{15/2}$ (550 nm) transitions of Er^{3+} ions, respectively, B is a constant, ΔE is the energy gap between the $^4S_{3/2}$ and $^2H_{11/2}$ states, k is the Boltzmann constant and T is the temperature, ΔE represents the energy separation between the $^2H_{11/2}$ and $^4S_{3/2}$ levels, k is the Boltzmann constant, and T stands for temperature. The temperature-dependent (FIR_1) shown in the figure demonstrates that FIR values increase with temperature.

Furthermore, to determine the feasibility of the synthesized microcrystals for thermometry, it is very important to analyze the relative and absolute sensitivity of the sensor, which is the ratio of change of the FIR with temperature, and which can be defined as follows:[54,57]

$$S_r = \frac{1}{\mathrm{FIR}} \frac{\mathrm{d(FIR)}}{\mathrm{d}T} = \mathrm{FIR} \times \frac{\Delta E}{kT^2} \quad (8)$$

$$S_a = \frac{d(\mathrm{FIR})}{\mathrm{d}T} \quad (9)$$

The sensor relative and absolute sensitivity, which was calculated from eqn (8), for the NSGM: 0.04Er^{3+} microcrystals as a function of temperature is shown in Fig. 10(b) the maximum Sr_1 was found for NSGM: 0.04 Er^{3+} at 298.15 K reaching 0.87% K^{-1} and the maximum S_{a_1} was found to be about 0.0059 K^{-1} at 488.15 K in the temperature range of interest. To determine its usefulness, the sensor sensitivity of the material is compared to that of other RE-doped phosphors (Table 1). As demonstrated in Table 1, the phosphor produced in this study performed well when compared to other host lattices such as phosphate,[58] fluoride,[55,59] oxide,[20,60] and tungsten.[61,62] Furthermore, based on the operational temperature range (298.15–488.15 K), NSGM: Er^{3+} phosphor has a high sensitivity temperature, which is promising for temperature sensor applications.

2.4.2. Temperature-dependent UC photoluminescence and temperature sensing. Fig. 10 demonstrates the UC emission spectra of NSGM: 0.04Er^{3+} excited by 975 nm in the wavelength region 500–700 nm, measured over a temperature range of 298.15 K to 488.15 K. The position and shape of the emission

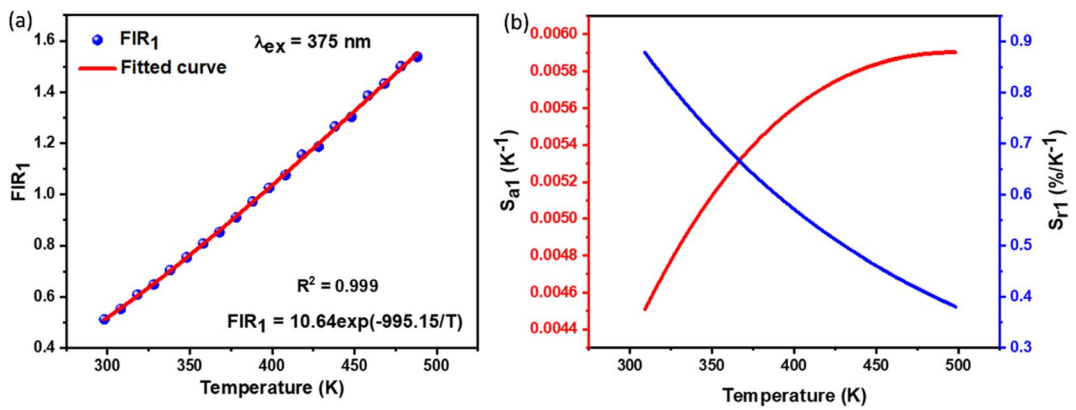

Fig. 9 (a) The determined FIR_1 values, (b) the absolute sensitivity and relative sensitivity with temperature of NSGM: 0.04Er^{3+} based on down-conversion.

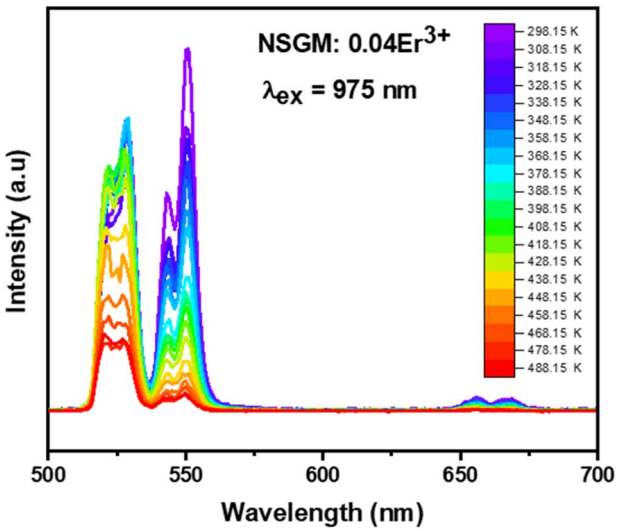

Fig. 10 Temperature-dependent up-conversion photoluminescence emission spectra of NSGM: 0.04 Er^{3+} under 975 nm excitation.

peaks remain unchanged at different temperatures. However, the emission intensity of peaks at 530 nm and 550 nm reacts differently. The electronic transitions responsible for these emissions are mentioned in the PL DC section and shown in the energy level diagram (Fig. 4(b)). The emission intensity of the 530 nm peak first increases with increasing temperature up, and after that, the emission intensity slowly decreases with increasing temperature. In contrast, the emission intensity of the 550 nm peak decreases steadily with increasing temperature. These patterns of emission intensity variation with temperature differ due to the thermal coupling of the $^4H_{11/2}$ and $^4S_{3/2}$ energy levels from which these transitions occur.

The ratio of the emission intensities of the thermally coupled energy levels changes with temperature, which is useful for temperature sensing applications. The energy levels $^2H_{11/2}$ and $^4S_{3/2}$ follow the Boltzmann distribution so that the fluorescence intensity ratio (FIR_2) between them is shown in eqn (7). The Fig. 10(a) shows the plot of the fluorescence intensity ratio (FIR_2) of two emission bands at 530 nm and 550 nm as a function of temperature for the NSGM: 0.04Er^{3+} phosphor. The sensitivity was calculated using (eqn (8)) and the plot is shown in Fig. 10(b). The maximum value of sensitivity relative (S_{r_2}) and absolute (S_{a_2}) are observed to be 0.63% K^{-1} at 298.15 K and 0.0036 K^{-1} at 488.15 K, respectively (Fig. 11).

In summary, both methods showed good performance for temperature detection, presenting high sensitivities compared to published works reported in Table 1, whether using down-conversion or up-conversion. However, down-conversion stood out in terms of relative sensitivity $S_{r_{max}} = 0.87\%\ K^{-1}$, indicating that it is more sensitive to temperature variations than up-conversion $S_{rmax} = 0.63\%\ K^{-1}$.

To assess the reliability of the measurements, the uncertainty in temperature determination (δT) was calculated using the following equation:[68]

$$\delta T = \frac{1}{S_R}\frac{\delta FIR}{FIR} \quad (10)$$

This uncertainty, δFIR, represents the limit of resolution or the relative uncertainty of the thermometric parameter, which is the smallest change in the ratio that can be experimentally observed. It is important to note that the limit of resolution depends on both the thermometer's performance and the characteristics of the experimental setup.[47] Therefore, to improve the limit of resolution, enhanced data acquisition methods and improvements in measurement performance can be considered. This could include adjustments such as increasing the integration time and using averaging of successive measurements to reduce experimental noise. To determine the detection limit, measurements were conducted at room temperature under similar conditions for the NSGM: Er^{3+} phosphor using both UC

Table 1 Temperature sensitivity comparison of the phosphors

Materials	Temperature range	S_{rmax}	Excitation wavelength	Ref.
$NaYF_4$: Er^{3+}/Yb^{3+}	93–673 K	0.0029 K^{-1} at 368 K	980 nm	59
YOF: Er^{3+}/Yb^{3+}	260–490 K	0.0060 K^{-1} at 490 K	980 nm	55
CaZnOS: Er^{3+}	303–603 K	0.0033 K^{-1} at 603.15 K	980 nm	63
$YNbO_4$: Er^{3+}/Yb^{3+}	298–673 K	0.0072 K^{-1} at 406 K	980 nm	20
La_2MoO_6: Er^{3+}	303–463 K	0.0097 K^{-1} at 460 K	379 nm	64
La_2O_3: Er^{3+}/Yb^{3+}	303–600 K	0.0091 K^{-1} at 303 K	980 nm	60
$Ba_5Gd_8Zn_4O_{21}$: Er^{3+}/Yb^{3+}	260–490 K	0.0032 K^{-1} at 490 K	980 nm	65
PKAZLF glass: Er^{3+}	298–773 K	0.0079 K^{-1} at 630 K	488 nm	66
$CaLa_2ZnO_5$: Er^{3+}/Yb^{3+}	298–513 K	0.0059 K^{-1} at 483 K	980 nm	67
YVO_4: Er^{3+}/Yb^{3+}	300–485 K	0.0116 K^{-1} at 380 K	980 nm	19
$YNbO_4$: Er^{3+}/Yb^{3+}	298–673 K	0.0072 K^{-1} at 406 K	980 nm	64
$AgLa(MoO_4)_2$: Er^{3+}/Yb^{3+}	300–510 K	0.018 K^{-1} at 480 K	980 nm	21
$NaZnPO_4$: $Er^{3+}/Yb^{3+}/Li^+$	300–603 K	0.0065 K^{-1} at 306 K	980 nm	58
$NaZnPO_4$: $Er^{3+}/Yb^{3+}/Ba^{2+}$	300–523 K	0.0043 K^{-1} at 523 K	970 nm	58
$CaWO_4$: Er^{3+}/Yb^{3+}	294–923 K	0.0092 K^{-1} at 455 K	980 nm	61
$SrWO_4$: Er^{3+}/Yb^{3+}	300–518 K	0.014 K^{-1} at 403 K	980 nm	62
NSGM: Er^{3+}	298.15–488.15 K	0.0087 K^{-1} at 298.15 K	375 nm	**This work**
NSGM: Er^{3+}	298.15–488.15 K	0.0063 K^{-1} at 298.15 K	975 nm	**This work**

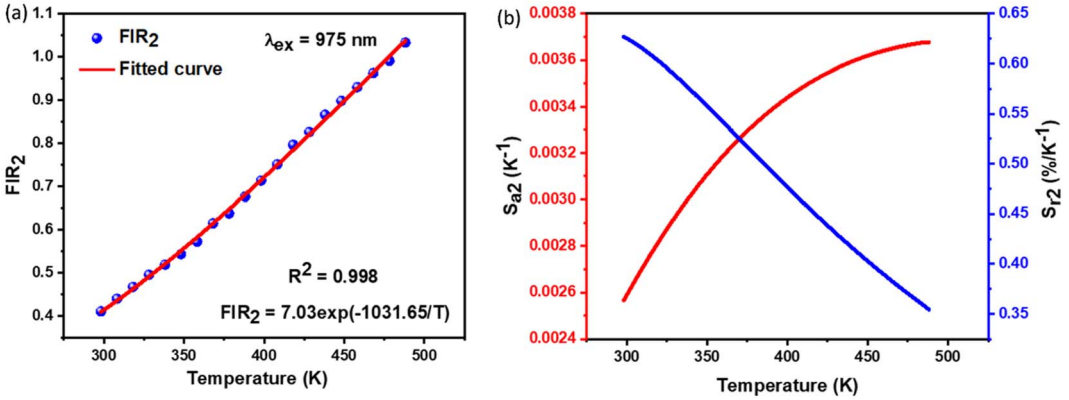

Fig. 11 (a) The determined FIR_2 values, (b) the absolute sensitivity and relative sensitivity with temperature of NSGM: $0.04Er^{3+}$ based on up-conversion.

and DC excitation. The results are presented as histograms in the (Fig. S_3(a) and (b)†). The FIR uncertainty (δFIR) was obtained by calculating the standard deviation of the statistical distribution for NSGM: $0.04Er^{3+}$, yielding values of 0.0010 and 0.0013 for FIR_1 and FIR_2, respectively. Using equation (eqn (10)), all δT (Fig. 12(a) and (b)) uncertainty values are below 0.50 K. This indicates that the NSGM: $0.04Er^{3+}$ microcrystals exhibit high accuracy across this entire temperature range.

The repeatability (R) of the sample must be assessed to establish if the crystals are an effective thermal probe. The following equation may be used to determine this parameter:[69]

$$R_p(100\%) = \left(1 - \frac{\max|FIR_c - FIR_{c_i}|}{FIR_c}\right) \times 100 \qquad (11)$$

where $M_i(T)_c$ is the measured parameter (FIR or band centroid) in the ith cycle and $M(T)_c$is the mean value of the $M(T)_c$ over 10 cycles. The FIR measurement was performed five times in a succession without altering the experimental equipment. Fig. 13(a) and (b) shows the cycle measurements of NSGM: $0.04Er^{3+}$ generated for emission-based DC and UC, respectively. The calculated value of R (more than 98%) indicates that the NSGM doped Er^{3+} manufactured have acceptable thermal repeatability.

2.5. Optical heating study. In order to investigate the optical heating effect in Er^{3+} doped NSGM phosphor caused by the laser excitation 975 nm, the green UC emission spectra were recorded in the 500–700 nm range at various excitation power density (11.52 to 42.12 W cm^{-2}) shown in Fig. S_4.† The laser beam was focused on the sample surface within 10 mm^2 area. Variation in the intensity of $^2H_{11/2}/^4I_{15/2}$ and $^4S_{3/2}/^4I_{15/2}$ transitions is not same for the sample due to the change in their populations in the corresponding levels. This dissimilar variation of two transitions gives rise to the variation of FIR with excitation power. The FIR (I_H/I_S) was calculated with excitation power density for the sample and the plot is shown in Fig. 14(a).

It is observed that on increasing the power density from 11.52 to 42.12 W cm^{-2}, the FIR value increases. This indicates that internal sample temperature increases with laser power excitation. A larger variation of FIR value indicates larger heating of material. Thus, it is concluded that laser excitation generates heat inside the sample. The variation in temperature as a function of sample power is essentially due to the energy absorbed by the crystalline powders and transferred as heat through non-radiative channels.[70] This optical heating

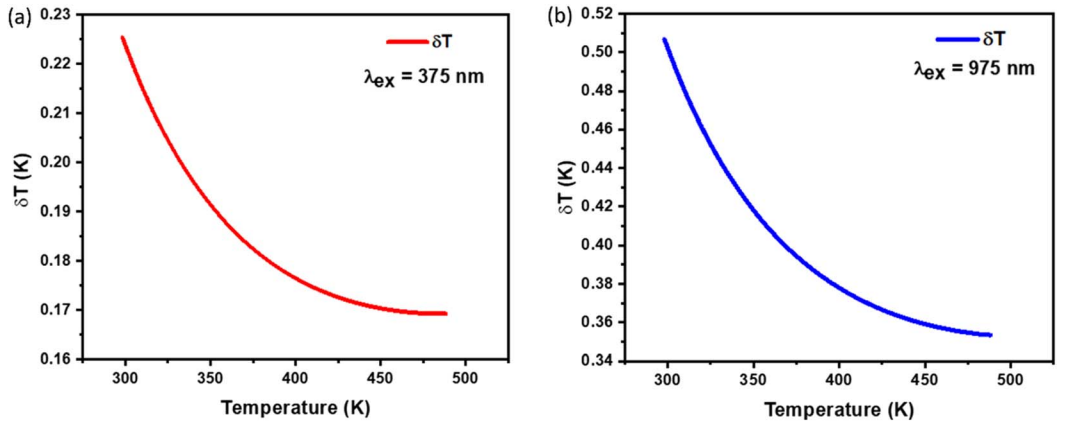

Fig. 12 Temperature resolution values δT, corresponding to (a) FIR_1 (DC), (b) FIR_2 (UC) for NSGM: $0.04Er^{3+}$.

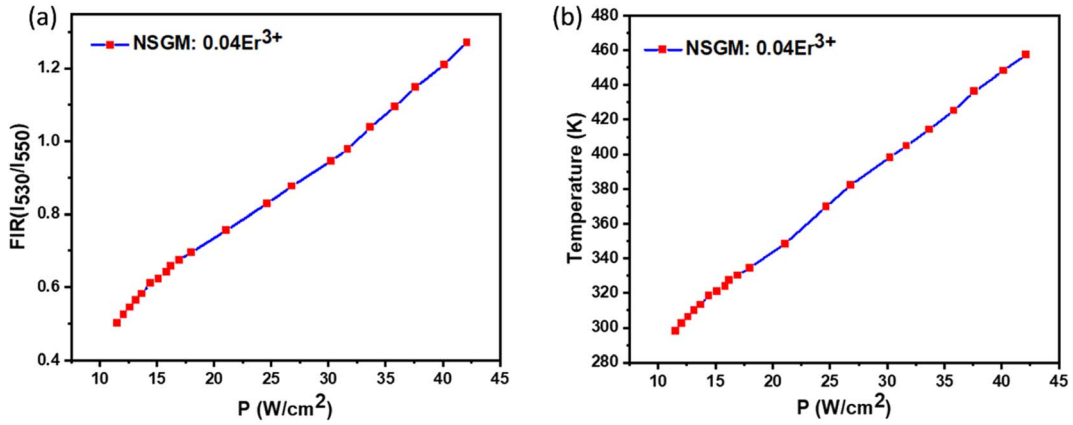

Fig. 13 Repeatability assessment (*R*) (a) and (b) for NSGM: $0.04Er^{3+}$ for (DC) and (UC), respectively.

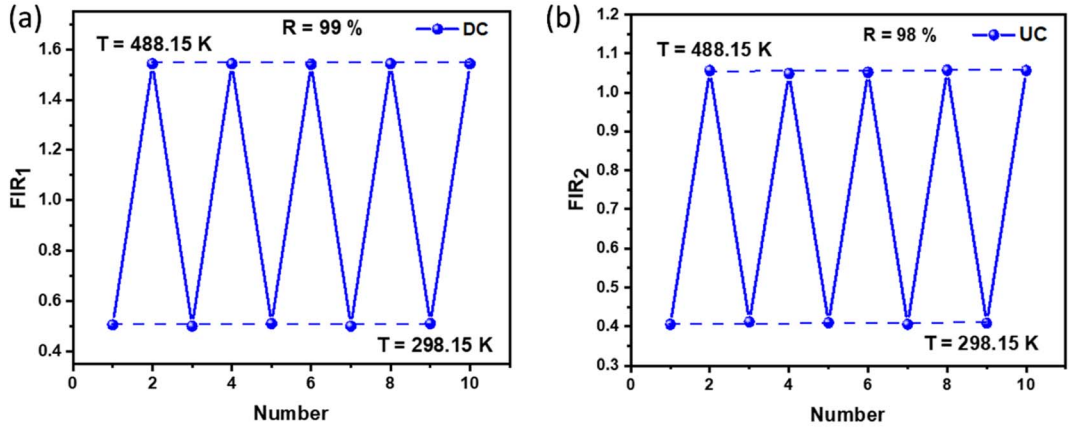

Fig. 14 Evolution of FIR (a) and temperature (b) as a function of power densities under excitation at 975 nm.

generated by laser excitation can be calculated using (eqn (8)), which is transformed into the following form:

$$T = \left(\frac{\Delta E}{k}\right)\left[\frac{1}{\{\ln(B) - \ln(\mathrm{FIR})\}}\right] \quad (12)$$

where, all the terms have their usual meanings. Using the ΔE and B values obtained from the temperature sensing study ($\Delta E = 670.15\ \mathrm{cm}^{-1}$ and $B = 7.03$), along with the FIR values corresponding to various power densities, the temperature increase of the sample was calculated using (eqn (12)). The sample temperature of the phosphor *versus* increasing power density is shown in Fig. 14(b). The internal sample temperature is found to increase with excitation power, reaches to 298 to 457 K, for Er^{3+} doped NSGM for the same pump power variation from 11.52 to 42.12 W cm^{-2}.[71,72] The heat generated in the sample is due to the non-radiative relaxation process and crystalline nature of the phosphor powders.[73] When energy cannot be fully utilized in radiative transitions, excess energy will lead to phonon-assisted non-radiative transitions, resulting in a rise in temperature.[74] The result suggests that Er^{3+} doped NSGM phosphor is capable of transferring the NIR laser excitation pump power into heat and act as an optical heater which could be useful for photo-thermal therapy.

2.6. Conclusion. In summary, Er^{3+}-doped (NSGM) green phosphors were successfully synthesized through the standard solid-state reaction method. XRD analysis confirmed the formation of a well-crystalline tetragonal phase of NSGM: Er^{3+} with the $I4_1/a$ space group (88), and SEM analysis revealed an average particle size of approximately 2 μm. Absorption measurements indicated the formation of the molybdate host, evidenced by the characteristic band of $MoO4^{2-}$ groups in the visible region. The energy gap values for NSGM: 0.04 Er^{3+} were determined to be 3.59 eV. Under excitation at 375 and 975 nm, the dominant peaks at 530 and 550 nm corresponded to the $^2H_{11/2}$, $^4S_{3/2} \rightarrow 4_{I15/2}$ transitions, resulting in green light emission. Chromaticity parameter studies indicated a thermally stable cold emission in the green spectrum, with color purities of approximately 98.76% and 80.74% for DC and UC conversion, respectively. Furthermore, the DC and UC temperature-sensing properties of the phosphors were examined by analyzing the fluorescence intensity ratio between the $^2H_{11/2}$, $^4S_{3/2} \rightarrow {}^4I_{15/2}$ transitions within the temperature range of 298.15 to 488.15 K. NSGM: $0.04Er^{3+}$ demonstrated higher sensitivity to

temperature, with a maximum relative sensitivity of 0.87%/K^{-1} under 375 nm light excitation. Conversely, under 975 nm light excitation, NSGM: 0.04Er^{3+} exhibited a maximum relative sensitivity of 0.63%/K^{-1} within the same temperature range. Luminescence thermometry showcased outstanding accuracy in temperature measurement, with a calculated temperature uncertainty (δT) of less than 0.50 K and repeatability (R) exceeding 98%. This exceptional precision highlights the potential of luminescence thermometry as a high-precision optical sensing technique. These results position this material as promising candidate for temperature sensing applications. Additionally, laser-induced optical heating inside the sample was quantified using the appropriate formula, revealing a temperature increase of around 457 K with an increased power density of up to 42.12 W cm^{-2}. This observation suggests that NSGM: 0.04Er^{3+} holds promise for photo-thermal therapy.

Conflicts of interest

There are no conflicts to declare.

References

1 K. Saidi, C. Hernández-Álvarez, M. Runowski, M. Dammak and I. Rafael Martín Benenzuela, *ACS Appl. Nano Mater.*, 2023, **6**, 19431–19442.
2 R. Gopal and J. Manam, *Appl. Phys. A*, 2022, **128**, 772.
3 A. Kumar and J. Manam, *Ceram. Int.*, 2022, **48**, 13615–13625.
4 Z. E. A. A. Taleb, K. Saidi and M. Dammak, *Dalton Trans.*, 2023, **52**, 18069–18081.
5 B. P. Singh, A. K. Parchur, R. S. Ningthoujam, A. A. Ansari, P. Singh and S. B. Rai, *Dalton Trans.*, 2014, **43**, 4770–4778.
6 Z. E. A. A. Taleb, K. Saidi, M. Dammak, D. Przybylska and T. Grzyb, *Dalton Trans.*, 2023, **52**, 4954–4963.
7 S. Sinha, M. K. Mahata, K. Kumar, S. P. Tiwari and V. K. Rai, *Spectrochim. Acta, Part A*, 2017, **173**, 369–375.
8 Y. Jin, J. Zhang, S. Lü, H. Zhao, X. Zhang and X. Wang, *J. Phys. Chem. C*, 2008, **112**, 5860–5864.
9 J. H. Chung, J. H. Ryu, J. W. Eun, J. H. Lee, S. Y. Lee, T. H. Heo, B. G. Choi and K. B. Shim, *J. Alloys Compd.*, 2012, **522**, 30–34.
10 Y. Zhou, X.-H. He and B. Yan, *Opt. Mater.*, 2014, **36**, 602–607.
11 S. Vidya, S. Solomon and K. Thomas, *Phys. Status Solidi*, 2012, **209**, 1067–1074, accessed December 13, 2023.
12 C. Hernández-Álvarez, G. Brito-Santos, I. R. Martín, J. Sanchiz, K. Saidi, K. Soler-Carracedo, Ł. Marciniak and M. Runowski, *J. Mater. Chem. C*, 2023, **11**, 10221–10229.
13 X. Liu, J. Wang, R. Lei, S. Zhao, F. Huang, D. Deng and S. Xu, *Sens. Actuators, A*, 2020, **315**, 112287.
14 K. Saidi, M. Dammak, K. Soler-Carracedo and I. R. Martín, *J. Alloys Compd.*, 2022, **891**, 161993.
15 A. Torquato, R. A. de Oliveira, T. O. Sales, G. Y. Poirier, G. Batista, F. C. Cassanjes, C. Jacinto and M. R. Dousti, *Opt. Mater.*, 2021, **112**, 110723.
16 S. Li, W. Wang, X. Wei, L. Li, Q. Zhang, Y. Li and Y. Pan, *Opt. Mater.*, 2021, **113**, 110840.
17 K. Saidi, I. Kachou, K. Soler-Carracedo, M. Dammak and I. R. Martín, *ACS Appl. Nano Mater.*, 2023, **6**, 17681–17690.
18 M. K. Mahata, K. Kumar and V. K. Rai, *Spectrochim. Acta, Part A*, 2014, **124**, 285–291.
19 M. K. Mahata, K. Kumar and V. Kr. Rai, *Sens. Actuators, B*, 2015, **209**, 775–780.
20 Y. Tian, Y. Tian, P. Huang, L. Wang, Q. Shi and C. Cui, *Chem. Eng. J.*, 2016, **297**, 26–34.
21 T. Li, C. Guo, S. Zhou, C. Duan and M. Yin, *J. Am. Ceram. Soc.*, 2015, **98**, 2812–2816.
22 Y. K. Kshetri, B. Chaudhary, T.-H. Kim, H. S. Kim and S. W. Lee, *J. Eur. Ceram. Soc.*, 2021, **41**, 2400–2406.
23 H. Gong, X. Peng, G. A. Ashraf, F. Hu, R. Wei and H. Guo, *Ceram. Int.*, 2022, **48**, 4023–4030.
24 J. Hu, X. Zhang, H. Zheng, F. Lu, X. Peng, R. Wei, F. Hu and H. Guo, *Ceram. Int.*, 2022, **48**, 3051–3058.
25 L. Li, P. Yang, W. Xia, Y. Wang, F. Ling, Z. Cao, S. Jiang, G. Xiang, X. Zhou and Y. Wang, *Ceram. Int.*, 2021, **47**, 769–775.
26 Q. Zhang, L. Li, F. Liu, S. Li, X. Wei, W. Wang, H. Chen, Y. Pan and Y. Li, *J. Solid State Chem.*, 2022, **308**, 122927.
27 M. Rajendran and S. Vaidyanathan, *New J. Chem.*, 2020, **44**, 5354–5365.
28 Y. Jin, J. Zhang, S. Lü, H. Zhao, X. Zhang and X. Wang, *J. Phys. Chem. C*, 2008, **112**, 5860–5864.
29 S. Sinha, M. K. Mahata, H. C. Swart, A. Kumar and K. Kumar, *New J. Chem.*, 2017, **41**, 5362–5372.
30 M. Rajendran, R. Devi, S. Mund, K. Singh and S. Vaidyanathan, *J. Mater. Chem. C*, 2021, **9**, 15034–15046.
31 L. Li, Y. Pan, X. Zhou, C. Zhao, Y. Wang, S. Jiang, A. Suchocki and M. G. Brik, *J. Alloys Compd.*, 2016, **685**, 917–926.
32 B. Han, J. Zhang, Z. Wang, Y. Liu and H. Shi, *J. Lumin.*, 2014, **149**, 150–154.
33 X. Chai, J. Li, Y. Zhang, X. Wang, Y. Li and X. Yao, *RSC Adv.*, 2016, **6**, 64072–64078.
34 G. S. R. Raju, E. Pavitra and J. S. Yu, *Dalton Trans.*, 2014, **43**, 9766–9776.
35 S. Zeng, H. Wang, W. Lu, Z. Yi, L. Rao, H. Liu and J. Hao, *Biomaterials*, 2014, **35**, 2934–2941.
36 X. Huang, *J. Mater. Sci.*, 2016, **51**, 3490–3499.
37 P. Du, L. Luo and J. S. Yu, *Ceram. Int.*, 2016, **42**, 5635–5641.
38 A. Verma and S. K. Sharma, *Ceram. Int.*, 2017, **43**, 8879–8885.
39 S. Sinha and K. Kumar, *Opt. Mater.*, 2018, **75**, 770–780.
40 A. Kumar and J. Manam, *J. Alloys Compd.*, 2020, **829**, 154610.
41 P. Rohilla and A. S. Rao, *Mater. Res. Bull.*, 2022, **150**, 111753.
42 M. K. Pradhan and S. Dash, *J. Rare Earths*, 2022, **40**, 1837–1848.
43 R. S. Yadav, M. Rai, S. B. Rai and S. J. Dhoble, *Prog. Solid State Chem.*, 2020, **57**, 100267.
44 J. Yang, P. He, Y. Xie, Q. Chen, Q. Dong, W. Nie, F. Yang, W. Wang, F. Du, J. Peng and X. Ye, *J. Alloys Compd.*, 2022, **903**, 163815.
45 X. Feng, F. Long, B. Wang, Z. Weng, X. Wang, Y. Li and H. Ju, *Inorg. Chem. Commun.*, 2022, **137**, 109180.
46 M. Runowski, A. Shyichuk, A. Tymiński, T. Grzyb, V. Lavín and S. Lis, *ACS Appl. Mater. Interfaces*, 2018, **10**, 17269–17279.

47 K. Soler-Carracedo, I. R. Martín, F. Lahoz, H. C. Vasconcelos, A. D. Lozano-Gorrín, L. L. Martín and F. Paz-Buclatin, *J. Alloys Compd.*, 2020, **847**, 156541.
48 S. Ryszczyńska, K. Trejgis, Ł. Marciniak and T. Grzyb, *ACS Appl. Nano Mater.*, 2021, **4**, 10438–10448.
49 K. Annapoorani, N. Suriya Murthy, T. R. Ravindran and K. Marimuthu, *J. Lumin.*, 2016, **171**, 19–26.
50 X. Wang, X. Li, L. Cheng, S. Xu, J. Sun, J. Zhang, X. Zhang, X. Yang and B. Chen, *RSC Adv.*, 2017, **7**, 23751–23758.
51 D. L. Silva, R. S. Pugina and J. M. Almeida Caiut, *J. Lumin.*, 2022, **243**, 118639.
52 C. Zhao, Y. Gao, T. Song, J. Wang and J. Qiu, *J. Phys. Chem. Lett.*, 2023, **14**, 9011–9018.
53 A. Kumar and J. Manam, *Opt. Mater.*, 2019, **96**, 109373.
54 B. Dong, B. Cao, Y. He, Z. Liu, Z. Li and Z. Feng, *Adv. Mater.*, 2012, **24**, 1987–1993.
55 H. Suo, C. Guo, J. Zheng, B. Zhou, C. Ma, X. Zhao, T. Li, P. Guo and E. M. Goldys, *ACS Appl. Mater. Interfaces*, 2016, **8**, 30312–30319.
56 D. Chen, Z. Wang, Y. Zhou, P. Huang and Z. Ji, *J. Alloys Compd.*, 2015, **646**, 339–344.
57 C. D. S. Brites, P. P. Lima, N. J. O. Silva, A. Millán, V. S. Amaral, F. Palacio and L. D. Carlos, *Nanoscale*, 2012, **4**, 4799–4829.
58 L. Mukhopadhyay, V. K. Rai, R. Bokolia and K. Sreenivas, *J. Lumin.*, 2017, **187**, 368–377.
59 P. Du, L. Luo and J. Su Yu, *RSC Adv.*, 2016, **6**, 94539–94546.
60 R. Dey and V. K. Rai, *Dalton Trans.*, 2014, **43**, 111–118.
61 W. Xu, X. Gao, L. Zheng, P. Wang, Z. Zhang and W. Cao, *Appl. Phys. Express*, 2012, **5**, 072201.
62 A. Pandey, V. K. Rai, V. Kumar, V. Kumar and H. C. Swart, *Sens. Actuators, B*, 2015, **209**, 352–358.
63 H. Zhang, D. Peng, W. Wang, L. Dong and C. Pan, *J. Phys. Chem. C*, 2015, **119**, 28136–28142.
64 P. Du and J. S. Yu, *Chem. Eng. J.*, 2017, **327**, 109–119.
65 H. Suo, C. Guo and T. Li, *J. Phys. Chem. C*, 2016, **120**, 2914–2924.
66 N. Vijaya, P. Babu, V. Venkatramu, C. K. Jayasankar, S. F. León-Luis, U. R. Rodríguez-Mendoza, I. R. Martín and V. Lavín, *Sens. Actuators, B*, 2013, **186**, 156–164.
67 L. Li, C. Guo, S. Jiang, D. K. Agrawal and T. Li, *RSC Adv.*, 2014, **4**, 6391.
68 K. Saidi, W. Chaabani and M. Dammak, *RSC Adv.*, 2021, **11**, 30926–30936.
69 J. Zhu, T. Yang, H. Li, Y. Xiang, R. Song, H. Zhang and B. Wang, *Chem. Eng. J.*, 2023, **471**, 144550.
70 R. Dey, A. Pandey and V. K. Rai, *Sens. Actuators, B*, 2014, **190**, 512–515.
71 K. Nigoghossian, S. Ouellet, J. Plain, Y. Messaddeq, D. Boudreau and S. J. L. Ribeiro, *J. Mater. Chem. B*, 2017, **5**, 7109–7117.
72 S. Rohani, M. Quintanilla, S. Tuccio, F. De Angelis, E. Cantelar, A. O. Govorov, L. Razzari and F. Vetrone, *Adv. Opt. Mater.*, 2015, **3**, 1606–1613.
73 Q. Qiang and Y. Wang, *Front. Chem.*, 2019, **7**, 425.
74 S. Xiang, B. Chen, J. Zhang, X. Li, J. Sun, H. Zheng, Z. Wu, H. Zhong, H. Yu and H. Xia, *Opt. Mater. Express*, 2014, **4**, 1966–1980.